Coulomb drag in metallic twisted bilayer graphene

Federico Escudero* and Juan Sebastián Ardenghi
Departamento de Física, Universidad Nacional del Sur, Av. Alem 1253, B8000 Bahía Blanca, Argentina and Instituto de Física del Sur, Conicet, Av. Alem 1253, B8000 Bahía Blanca, Argentina

(Received 24 August 2023; accepted 27 September 2023; published 10 October 2023)

Strongly correlated phases in twisted bilayer graphene (TBG) typically arise as transitions from a state in which the system behaves as a normal metal. In such a metallic regime, electron-electron interactions usually only play a subleading role in transport measurements compared with the dominant scattering mechanism. Here, we propose and theoretically study an exception to this based on a Coulomb drag setup between two metallic TBGs separated so that they only couple through many-body interactions. We find that, by solely varying the twist angle equally in both TBGs, the drag resistivity exhibits a unique maximum as the system crosses over from a degenerate to a nondegenerate regime. When the twist angles in each TBG differ, we find an anomalous drag resistivity characterized by the appearance of multiple peaks. We show that this behavior can be related to the dependence of the rectification function on the twist angle.

DOI: 10.1103/PhysRevB.108.165409

I. INTRODUCTION

Recently, several experiments have shown the existence of numerous correlated phases in twisted bilayer graphene (TBG) around a magic angle $\theta_M \sim 1.05^\circ$, such as unconventional superconductivity and metal-insulator transitions [1–6]. These phenomena are thought to arise from electronic interactions that are greatly enhanced as the bands become flat at the magic angle [7–11]. The relation of these interactions with external parameters, such as the temperature or the carrier density, determines the state of the system. Consequently, much effort has been made to elucidate the transport properties of TBG due to many-body interactions [12–14]. A particular but relevant case is the normal metal state of TBG, which usually occurs at temperatures above which the superconductivity is observed [15,16]. The study of many-body effects in metallic TBG may thus help us understand the origin and nature of the correlated phases. However, although it is clear that electron-electron interactions play a major role in the rich phase diagram of TBG, their role within its normal metallic state is less evident. In part, this is because in such regime many-body interactions often only play a subleading role in transport measurements compared with the dominant scattering mechanism [17–20].

In this paper, we propose a direct method to study many-body interactions within the metallic regime, based on a Coulomb drag effect between two TBGs that are closely spaced but such that no interlayer hopping between them is possible. Both TBGs thus only couple through long-range Coulomb interactions. The drag effect arises when an external electric current driven in one layer induces a voltage difference in another closely spaced layer [21,22]. Typically, such an effect depends directly on the many-body interlayer interactions; the main mechanism is the Coulomb interaction, but phonon- or photon-mediated interactions may also contribute, especially at large interlayer separations [23–26]. The drag resistivity, i.e., the ratio between the applied current in the active layer and the voltage induced in the passive layer, reflects the response of the system due to the interlayer interactions as well as the temperature and carrier density in each layer [27]. Thus, Coulomb drag measurements between two metallic TBGs may allow one to elucidate properties of the electron-electron interactions in the system, to a degree that is not directly available in transport measurements carried out over a single TBG.

Here, we particularly focus on the drag at low temperatures and carrier densities, where the transport in metallic TBG is dominated by disorder and phonons [28,29]. We find that the drag resistivity ρ_D depends strongly on the angle-dependent Fermi velocity $v^\star$ in three general aspects: (i) the renormalization of the coupling constant $\alpha^\star \propto 1/v^\star$; (ii) the relation between the chemical potential μ and the temperature T, which in turn determines the regime of the system; and (iii) the interplay between intraband ($\omega < v^\star q$) and interband ($\omega > v^\star q$) scattering. When both TBGs have the same twist angle, the drag effect follows a conventional behavior in which, as the system crosses over from a degenerate to a nondegenerate regime, the drag resistivity peaks around $\mu/k_B T \sim 2$. However, when the twist angles are different, we find that the drag resistivity follows a nontrivial behavior, characterized by the appearance of several peaks. The shape of these peaks depends strongly on the twist difference as well as the temperature, carrier density, and distance between the TBGs. A qualitative explanation is given in terms of the angle dependence of the nonlinear susceptibility (NLS).

This work is organized as follows: In Sec. II, we describe the theoretical model used to study the Coulomb drag between two metallic TBGs, both of which are described by a two-band model within the Dirac approximation. Semianalytical

*federico.escudero@uns.edu.ar

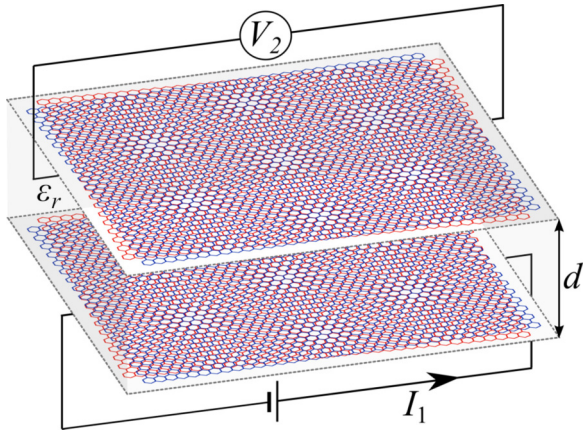

FIG. 1. Schematic setup to study the Coulomb drag between two twisted bilayer graphenes (TBGs). The TBGs are assumed to be separated by a dielectric medium by a distance d, so that no tunneling between them is possible. Electrons on each TBG can only interact through long-range many-body interactions. In a drag configuration, these interactions can induce a voltage difference V_2 in one TBG if a current I_1 is driven in the other TBG. The drag resistivity is determined by the ratio $\rho_D \propto V_2/I_1$.

expressions are obtained to compute the NLS, considering the full energy dependence of the scattering time in TBG, with contributions of both gauge phonons and charged impurities. The dynamically screened Coulomb interaction is obtained within the random phase approximation (RPA). In Sec. III, we present and discuss the numerical results for the drag resistivity, in the cases of equal twist angle in both TBGs and different twist angles. In the latter case, we provide an intuitive explanation for the observed anomalous drag behavior based on how the product of two nonlinear susceptibilities changes, depending on the difference between the twist angles. Finally, our conclusions follow in Sec. IV.

II. THEORETICAL MODEL

A. Proposed setup

The schematic drag setup is shown in Fig. 1. The two TBGs are separated so that no tunneling between them is possible, and they interact with one another only through long-range Coulomb interactions. These interactions can induce a voltage in one TBG (referred to as *passive* TBG) if a current is driven through the other TBG (referred to as *active* TBG). Throughout this paper, we assume that the twist angle in each TBG can be varied independently. Although this experimental configuration has not yet been realized, it seems feasible given the recent advances in fabricating moiré heterostructures [30–35].

The leading-order contribution to the drag conductivity σ_D can be calculated using either the diagrammatic approach [27,36,37] or the kinetic theory approach [38–41]. For a homogeneous system at a uniform temperature T, one gets

$$\sigma_D = \frac{e^2}{16\pi k_B T}\sum_{\mathbf{q}}\int_{-\infty}^{\infty} d\omega |U_{12}|^2 \frac{\Gamma_1\Gamma_2}{\sinh^2(\hbar\omega/2k_BT)}. \quad (1)$$

Here, $U_{12}(\mathbf{q},\omega)$ is the dynamically screened interlayer Coulomb interaction, and Γ_ℓ is the NLS in the $\ell = 1, 2$ TBG, projected along the current direction in the active TBG. From σ_D, the drag resistivity is obtained by inverting the 2×2 conductivity matrix $\rho_D \simeq -\sigma_D/\sigma_1\sigma_2$, where σ_ℓ ($\gg\sigma_D$) is the conductivity within each TBG.

B. Two-band Dirac model of TBG

In this paper, we restrict our analysis to the drag between two TBGs in the metallic regime. For low carrier densities, the electronic properties of metallic TBG are well captured by a two-band model in which electrons behave as massless chiral fermions with a Dirac-like Hamiltonian [7,8,10]:

$$\hat{H}_{0,\ell} = -i\hbar v_\ell^\star \int d\mathbf{r}\hat{\psi}_\ell^\dagger(\mathbf{r})\boldsymbol{\sigma}\cdot\nabla\hat{\psi}_\ell(\mathbf{r}), \quad (2)$$

with a renormalized Fermi-velocity [42]:

$$v_\ell^\star = v\frac{1-3\alpha_\ell^2}{1+6\gamma^2\alpha_\ell^2}, \quad (3)$$

where v is the Fermi velocity in monolayer graphene [43]. Here, $\alpha_\ell = w_1/\hbar v k_{\theta,\ell}$ and $2\gamma^2 = 1+(w_0/w_1)^2$, where $w_1 \simeq 0.11$ eV and $w_0 \simeq 0.8w_1$ are the hopping energies of AB/BA and AA stacking, respectively [44,45], while $k_{\theta,\ell} = 8\pi\sin(\theta_\ell/2)/3a$ is the wave vector magnitude of the moiré Brillouin zone ($a \simeq 2.46$ Å is the lattice constant in graphene). For low twist angles, close to (but not exactly at) the first magic angle $\theta_M \sim 1.05^\circ$, the two-band model remains a good approximation for carrier densities $n \lesssim 10^{11}$ cm^{-2} [28].

The field operators can be expanded in momentum space as $\hat{\psi}_\ell(\mathbf{r}) = A^{-1/2}\sum_{\mathbf{k},s} e^{i\mathbf{k}\cdot\mathbf{r}}\hat{c}_{\ell,\mathbf{k},s}u_{\mathbf{k},s}$, where A is the area of the system. The operator $\hat{c}_{\ell,\mathbf{k},s}$ annihilates an electron in the $\ell = 1, 2$ TBG, with momentum $\mathbf{k}$ in the $s = \pm$ band. The Dirac approximation requires $|\mathbf{k}| \ll k_\theta$. The pseudospinor $u_{\mathbf{k},s}^\dagger = (1 \quad se^{-i\varphi_\mathbf{k}})/\sqrt{2}$, where $\tan\varphi_\mathbf{k} = k_y/k_x$ comes from the sublattice structure in graphene [43,46]. Replacing the field operators $\hat{\psi}_\ell(\mathbf{r})$ in Eq. (2) leads to the energy operator $\hat{H}_{0,\ell} = \sum_{\mathbf{k},s}\epsilon_{\ell,\mathbf{k},s}\hat{c}_{\ell,\mathbf{k},s}^\dagger\hat{c}_{\ell,\mathbf{k},s}$, where $\epsilon_{\ell,\mathbf{k},s} = s\hbar v_\ell^\star|\mathbf{k}|$ is the dispersion relation in the s band. The pseudospinor $u_{\mathbf{k},s}$ yields the well-known chirality factor within the Dirac approximation:

$$F_{ss'}(\mathbf{k},\mathbf{q}) = |u_{\mathbf{k}+\mathbf{q},s'}^\dagger u_{\mathbf{k},s}|^2 = \frac{1+ss'\cos(\varphi_\mathbf{k}-\varphi_{\mathbf{k}+\mathbf{q}})}{2}. \quad (4)$$

C. Scattering time and conductivity

The conductivity σ_ℓ depends on the dominant scattering mechanism. In metallic TBG, at low temperatures, this scattering has, in general, nonnegligible contribution from impurities and phonons [20,29,47]. The latter comes from gauge phonons that are immune to the strong screening that arises in the flat bands of TBG around the magic angle [28].

For the impurity scattering, we consider long-range Coulomb disorder, considering the static screening within the RPA [48]:

$$\frac{1}{\tau_{\mathrm{i},\ell}} = 2\pi(\alpha_\ell^\star)^2 n_i v_\ell^\star k\int_0^\pi d\theta\frac{1-\cos^2\theta}{[2k\sin(\theta/2)+q_{T,\ell}]^2}. \quad (5)$$

Here, $\alpha_\ell^\star = e^2/4\pi\hbar\varepsilon_0\varepsilon_r v_\ell^\star$ is the coupling constant, n_i is the impurity density, and $q_{T,\ell} = q_{0T,\ell}\tilde{\Pi}_\ell(q,T)$ is the screened Thomas-Fermi (TF) momentum, where $q_{0T,\ell} = g\alpha_\ell^\star k_{F,\ell}$ ($g = 8$ is the flavor degeneracy in TBG), and

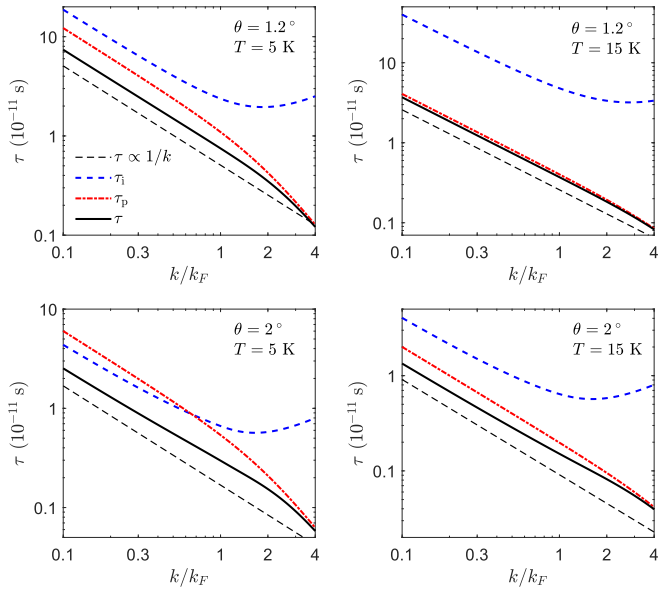

FIG. 2. Momentum dependence of the scattering time (ST) in metallic twisted bilayer graphene (TBG), for different twist angles and temperatures. Blue dashed line shows the ST $\tau_{\rm i}$ due to long-range screened charged impurities with density $n_i = 10^{10}$ cm^{-2}, red dot-dashed line the ST $\tau_{\rm p}$ due to gauge phonons, and solid black line the net ST $\tau^{-1} = \tau_{\rm i}^{-1} + \tau_{\rm p}^{-1}$. Black dashed line schematically shows a dependence $\tau \propto 1/k$. In all cases $n = 5 \times 10^{10}$ cm^{-2}.

$\tilde{\Pi}_\ell[q = 2k\sin(\theta/2), T]$ is the static polarization at finite temperatures [46]. For the phonon scattering, since we will restrict our analysis to twist angles for which the Fermi velocity is still much higher than the phonon velocities, we consider only the intraband scattering [20,29]. For gauge phonons, one then has [28,29]

$$\frac{1}{\tau_{{\rm p},\ell}} = \sum_\nu \frac{\zeta_\ell^2}{2h\rho c_\nu v_\ell^\star} \int_0^{2k} dq \frac{q^3}{k^2} \sqrt{1 - \left(\frac{q}{2k}\right)^2} \left(1 + 2n_{\ell,\mathbf{q},\nu}\right), \tag{6}$$

where the summation is over the two acoustic phonon branches (LA and TA), for which we assume an average velocity $c_\nu \simeq 2 \times 10^6$ cm/s (independent of the twist angle). Here, $\zeta_\ell = \beta_A v_\ell^\star / v \tan(\theta/2)$ is the coupling constant [49] ($\beta_A \sim 3.6$ eV), ρ is the mass density in monolayer graphene, and $n_{\ell,\mathbf{q},\nu}$ is the Bose-Einstein distribution.

Using the Matthiessen's rule, which is a good approximation at relatively large twist angles [50], the net scattering time is given by $\tau_\ell^{-1} = \tau_{{\rm i},\ell}^{-1} + \tau_{{\rm p},\ell}^{-1}$. Unless the temperature is very low and the twist angle is relatively large, τ_ℓ^{-1} is mostly determined by the phonon contribution, roughly yielding a momentum dependence $\tau_\ell \propto 1/k$ [28,29] (see Fig. 2).

Given the scattering time, the conductivity is then calculated as $\sigma_\ell = g e^2 (v_\ell^\star)^2 \sum_{\mathbf{k},s} \tau_\ell (-\partial f_{\ell,\mathbf{k},s}/\partial \epsilon_{\ell,\mathbf{k},s})$, where $f_{\ell,\mathbf{k},s}$ is the Fermi-Dirac distribution. The chemical potential μ_ℓ is obtained numerically from the equation for the carrier density, $n_\ell = (g/A)\sum_{\mathbf{k},s}[f_{\ell,\mathbf{k},s}(\mu_\ell) - f_{\ell,\mathbf{k},s}(\mu_\ell = 0)]$, which implies

$$n_\ell = \frac{g}{2\pi}\left(\frac{k_B T}{\hbar v_\ell^\star}\right)^2 [{\rm Li}_2(-e^{-\beta\mu_\ell}) - {\rm Li}_2(-e^{\beta\mu_\ell})], \tag{7}$$

where ${\rm Li}_2(x)$ is the dilogarithm function.

D. NLS

Within the two-band model of TBG, the NLS is calculated as [41,51,52]

$$\begin{aligned}\mathbf{\Gamma}_\ell(\mathbf{q},\omega) = -2\pi g \sum_{\mathbf{k},s,s'} (f_{\ell,\mathbf{k},s} - f_{\ell,\mathbf{k}+\mathbf{q},s'}) F_{ss'}(\mathbf{k},\mathbf{q}) \\ \times (\tau_{\ell,\mathbf{k}} \mathbf{v}_{\ell,\mathbf{k},s} - \tau_{\ell,\mathbf{k}+\mathbf{q}} \mathbf{v}_{\ell,\mathbf{k}+\mathbf{q},s'}) \\ \times \delta(\hbar\omega + \epsilon_{\ell,\mathbf{k},s} - \epsilon_{\ell,\mathbf{k}+\mathbf{q},s'}),\end{aligned} \tag{8}$$

where $\mathbf{v}_{\ell,\mathbf{k},s} = \hbar^{-1}\nabla\epsilon_{\ell,\mathbf{k},s}$ is the velocity vector. The NLS at finite temperatures, beyond the degenerate regime, is typically obtained by assuming a constant scattering time [27,53,54]. Since this would not capture the strong momentum-dependence of $\tau_{\ell,\mathbf{k}}$ in metallic TBG, we compute the NLS semianalytically by rather considering a scattering time of the form $\tau_\ell(|\mathbf{k}| = k)$, only imposing the restriction that it is isotropic [52]. After straightforward algebraic manipulations, we then find the general expression (see Appendix A):

$$\begin{aligned}\mathbf{\Gamma}_\ell(\mathbf{q},\omega > 0) = \frac{g}{4\pi\hbar} \frac{1}{\sqrt{|q^2 - \omega_\ell^2|}} \frac{\mathbf{q}}{q^2} [\Theta(q - \omega_\ell)\Gamma_{\ell,+}(q,\omega) \\ + \Theta(\omega_\ell - q)\Gamma_{\ell,-}(q,\omega)],\end{aligned} \tag{9}$$

where Θ is the step function, $\omega_\ell = \omega/v_\ell^\star$, and

$$\begin{aligned}\Gamma_{\ell,+}(q,\omega) = \sum_{s=\pm1} \int_{(q - s\omega_\ell)/2}^{\infty} dk \mathcal{F}_{\ell,s}(k,\omega)\mathcal{K}_{\ell,s}(k,q,\omega), \\ \Gamma_{\ell,-}(q,\omega) = \int_{(\omega_\ell - q)/2}^{(\omega_\ell + q)/2} dk \mathcal{F}_{\ell,-1}(k,\omega)\mathcal{K}_{\ell,-1}(k,q,\omega),\end{aligned} \tag{10}$$

with

$$\mathcal{F}_{\ell,s}(k,\omega) = f_\ell(k) + f_\ell(-k) - f_\ell(k + s\omega_\ell) - f_\ell(-k - s\omega_\ell), \tag{11}$$

$$\begin{aligned}\mathcal{K}_{\ell,s}(k,q,\omega) = \frac{s}{k}\sqrt{|(\omega_\ell + 2sk)^2 - q^2|} \\ \times \tau_\ell(k)\left(q^2 - \omega_\ell^2 - 2sk\omega_\ell\right).\end{aligned} \tag{12}$$

Semianalytical expressions for the NLS with an arbitrary energy-dependent scattering time were obtained in Ref. [27]. In the present case of TBG, the NLSs are calculated numerically at finite temperatures by using the full energy and temperature dependence of the scattering time, as given by Eqs. (5) and (6). We note that, in the final expression of the drag resistivity, the divergences in Eq. (9) when $q \to \omega_\ell$ (which comes from the fact that the dispersion relation is linear [22]) are cured when one considers the full dynamical screening of the interlayer interaction [52,55] (see Appendix B).

E. Many-body interactions

The electron-electron interactions in the proposed setup are described by the Hamiltonian:

$$\hat{H}_{\ell\ell'} = \frac{1}{2}\int d\mathbf{x} d\mathbf{y} \hat{\psi}_\ell^\dagger(\mathbf{x})\hat{\psi}_{\ell'}^\dagger(\mathbf{y}) V_{\ell\ell'}(\mathbf{x} - \mathbf{y})\hat{\psi}_{\ell'}(\mathbf{y})\hat{\psi}_\ell(\mathbf{x}), \tag{13}$$

where $V_{\ell\ell'}(\mathbf{r}) = (e^2/4\pi\varepsilon_0\varepsilon_r)/[\mathbf{r}^2 + (1 - \delta_{\ell\ell'})d^2]$ is the bare Coulomb potential. In principle, the interaction in Eq. (13)

can be treated perturbatively if the coupling constant is small [27,36]. For TGB embedded in a homogeneous dielectric medium of relative permitting ε_r, the coupling constant reads $\alpha_\ell^\star \sim \alpha_g(v/v_\ell^\star)$, where $\alpha_g \sim 2.2/\varepsilon_r$ is the coupling constant in monolayer graphene [43]. The value of α_g is expected to also depend on the quasiparticle renormalization due to intralayer many-body interactions, which tend to lower α_g [56]. In what follows, we set a bare value $\alpha_g = 0.3$, which roughly corresponds to $\alpha_g \sim 1.3/\varepsilon_r$ and a uniform boron nitride dielectric medium ($\varepsilon_r \sim 4$) [57]. Since the resulting coupling constant in TBG then becomes of the order of unity already at relatively low velocity renormalizations, we restrict our analysis to $\theta \gtrsim 1.2^\circ$. Although $\alpha_\ell^\star$ at low twist angles is clearly not small in the context of QED, it is still within the range found in most metals [58].

The dynamical screening is then calculated within the RPA by coupling the passive and active TBGs with a diagonal polarization matrix [36]. Assuming a drag setup with a homogeneous dielectric medium [53,59], the RPA yields the screened interlayer interaction $U_{12}(\mathbf{q},\omega) = V_{12}(q)/\varepsilon_{12}(\mathbf{q},\omega)$, with

$$\varepsilon_{12}(\mathbf{q},\omega) = [1 + V_{11}(q)\Pi_1(\mathbf{q},\omega)][1 + V_{22}(q)\Pi_2(\mathbf{q},\omega)] - V_{12}^2(q)\Pi_1(\mathbf{q},\omega)\Pi_2(\mathbf{q},\omega), \quad (14)$$

where $V_{\ell\ell'}(q) = (e^2/2\varepsilon_0\varepsilon_r)q^{-1}\exp[-qd(1-\delta_{\ell\ell'})]$ is the Fourier transform of the Coulomb potential, and $\Pi_\ell(\mathbf{q},\omega)$ is the dynamical polarization in the ℓ TBG:

$$\Pi_\ell(\mathbf{q},\omega) = -g\sum_{\mathbf{k},s,s'} \frac{(f_{\ell,\mathbf{k},s} - f_{\ell,\mathbf{k}+\mathbf{q},s'})F_{ss'}(\mathbf{k},\mathbf{q})}{\hbar\omega + \epsilon_{\ell,\mathbf{k},s} - \epsilon_{\ell,\mathbf{k}+\mathbf{q},s'} + i0^+}. \quad (15)$$

The polarization function gives the dependence of the screened interaction U_{12} on the twist angle in each TBG. Since electrons in TBG can crossover from a degenerate to a nongenerate regime as the twist angle decreases, it is essential to consider the dynamical screening at finite temperatures [27]. This naturally captures the role of plasmons in the drag, which are expected to become relevant when $T \gtrsim 0.2T_F$ [27,53,60], where T_F is the Fermi temperature. We compute $\Pi_\ell(\mathbf{q},\omega)$ numerically, at finite temperatures, by using the semianalytical expressions of Ref. [61] for the polarization operator in monolayer graphene and considering the twist angle by its leading-order renormalization of the Fermi velocity (Appendix B).

III. RESULTS AND DISCUSSION

A. Equal twist angles

Figure 3 shows the drag resistivity between two TBGs with the same twist angle θ. The observed behavior can be well explained by a crossover of the system from a degenerate to a nondegenerate regime [27,40,53,62]. Indeed, since the chemical potential μ increases as the Fermi velocity in each TBG increases, the ratio μ/k_BT scales with the twist angle, thus leading to the observed drag behavior. As small variations in θ can lead to relatively large changes in the Fermi velocity, the drag effect is highly sensitive to the exact twist angle in TBG. For instance, at $T = 15$ K, a twist decrease $\Delta\theta \sim 0.3^\circ$ already reduces ρ_D from its peak by more than one order of magnitude. Such reduction becomes even more pronounced

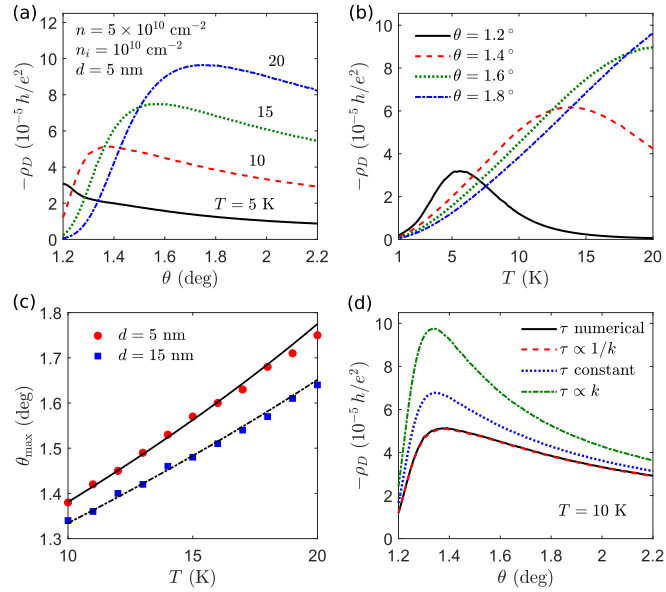

FIG. 3. (a) and (b) Drag resistivity for equal twist angles. The drag peaks as twisted bilayer graphene (TBG) crosses over from a degenerate to a nondegenerate regime. This can take place by solely lowering the twist angle. (c) Twist angle $\theta_{\max}$ at which the drag resistivity is maximum; dots are numerical results, and the lines are obtained from Eq. (16) by fixing the ratio $\beta\mu$ at 3.4 ($d = 5$ nm) and 2.8 ($d = 15$ nm), around which ρ_D peaks in each case. (d) Drag resistivity for different scattering times τ. The black solid line is the full numerical calculation using Eqs. (5) and (6).

at higher temperatures. A similar high sensibility to the twist angle is already seen in the resistivity at each TBG [28,50].

The peak of the drag resistivity generally occurs when $\beta\mu$ is of the order of unity [27,40]. The ratios $\beta\mu$ and $v^\star/v$ can be related through the carrier density Eq. (7). Replacing the renormalized velocity in Eq. (3) and solving for the twist angle yields

$$\theta \simeq \frac{\sqrt{3}w_1}{\hbar v k_D}\sqrt{\frac{1 + 2\gamma^2 F(\beta\mu)T/T_{Fg}}{1 - F(\beta\mu)T/T_{Fg}}}, \quad (16)$$

where $F(x) = \sqrt{g/2}[\mathrm{Li}_2(-e^{-x}) - \mathrm{Li}_2(-e^x)]^{1/2}$, $k_D = 4\pi/3a$, and $T_{Fg} = \hbar v\sqrt{\pi n}/k_B$ is the Fermi temperature in monolayer graphene. Over relatively small ranges of temperatures, as considered in Fig. 3, the value of $\beta\mu$ at which ρ_D peaks depends weakly on T and n [27]. Thus, to leading order in T, the maximum of the drag resistivity can be determined by treating $\beta\mu$ as constant, yielding the relation $v^\star_{\max}/v \propto T/\sqrt{n}$. Equation (16) is shown in solid and dashed lines in Fig. 3(c) for fixed values of $\beta\mu$. The small departure of Eq. (16) from the numerical results is due to the small temperature dependence of the value of $\beta\mu$ at which the drag peaks. From an experimental point of view, the location of the maxima of the drag resistivity can be used to obtain, for example, information about the hopping parameters w_0 and w_1.

Figure 3(d) shows that the overall drag behavior, in the case of equal twist angle, is largely independent of the scattering time within each TBG. Any particular energy dependence of the scattering mechanism appears to mainly modify the

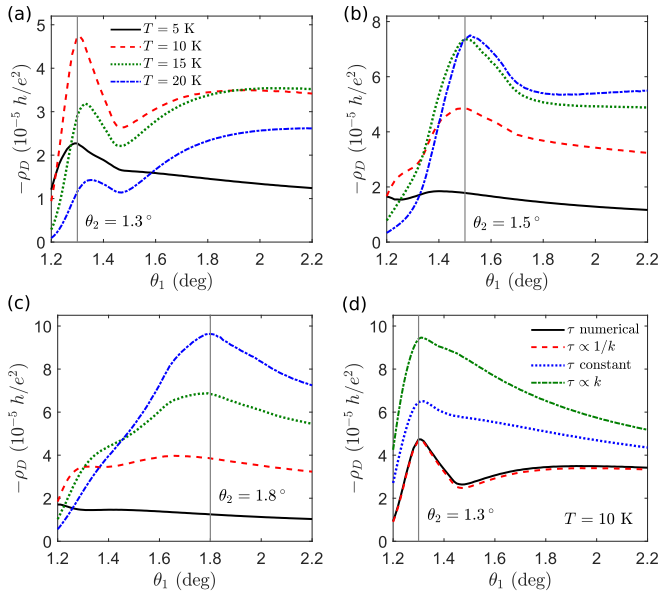

FIG. 4. (a)–(c) Drag resistivity for different twist angles. In each case, the twist angle θ_2 in one twisted bilayer graphene (TBG) is fixed (thin vertical line) as the other θ_1 is varied. All other parameters as in Fig. 3. (d) Drag resistivity for different scattering times. A nonmonotonic behavior appears due to the particular momentum-dependence of τ in metallic TBG.

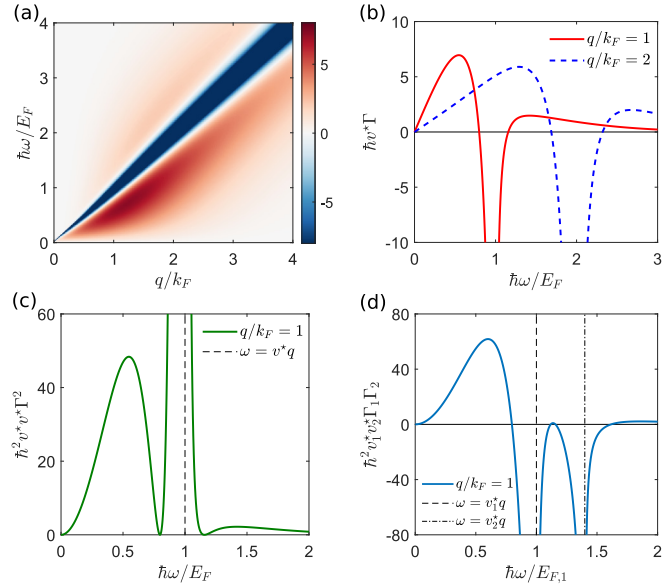

FIG. 5. Nonlinear susceptibility (NLS) behavior in twisted bilayer graphene (TBG), for $\theta = 1.3^\circ$, $T = 10$ K, $n = 5 \times 10^{10}$ cm^{-2}, and $n_i = 10^{10}$ cm^{-2}. (a) shows a density plot of the scaled NLS $\hbar v^\star \Gamma$, while (b) shows cuts on the momentum plane. In both cases, it can be seen that the NLS changes sign at each side of the line $v^\star q = \omega$. (c) and (d) Result of multiplying two NLSs with equal and different twist angles, respectively. In the first case, the result is always positive value and peaks only at $v^\star q = \omega$. In the second case, the result can be negative at certain regions and has two distinctive peaks at $v_1^\star q = \omega$ and $v_2^\star q = \omega$.

magnitude of the drag resistivity, particularly around its peak, but it does not modify where such a unique peak occurs (around $\mu/k_B T \sim 2$ [27,40]). This can be traced to the fact that the drag resistivity comes from a ratio $\sim \sigma_D/\sigma_1\sigma_2$ in which all conductivities depend directly on the scattering time, in such a way that the effect of $\tau_{\mathbf{k}}$ tends to be compensated in ρ_D [27,51,52]. Note that this is not the case for the drag conductivity which, as occurs with the conductivities $\sigma_{1,2}$, can depend strongly on the scattering mechanism [28].

B. Different twist angles

The behavior of the drag resistivity changes drastically when the TBGs have different twist angle. Figure 4 shows ρ_D as a function of the twist angle θ_1 in one TBG, when the twist angle θ_2 in the other TBG is kept fixed. In general, we observe multiple peaks in the drag resistivity, which depend nontrivially on other parameters of the system, such as the temperature, carrier density, and interlayer separation. The maximum of ρ_D always occurs around $\theta_1 \sim \theta_2$, albeit with a slight shift as the temperature increases. A distinctive minimum in the drag resistivity is seen for $\theta_1 > \theta_2$ only when the temperature and the twist angles are relatively low, such that one TBG is at least within a nondegenerate regime. As we discuss in detail below, the observed behavior can be related to an interplay between the dominant scattering mechanisms within each TBG and the twist dependence of the response functions Γ_ℓ.

The latter is directly reflected in the product $\sim\Gamma_1\Gamma_2$ in Eq. (1). Each NLS is a piecewise function that changes quite abruptly at $v_\ell^\star q = \omega$, which roughly divides the interband and intraband scattering regimes, cf. Eq. (9). As a result, the product of two NLSs can be markedly different depending on the twist angle in each TBG. The behavior of ρ_D is dictated by which layer has the larger twist angle. Furthermore, it is also strongly influenced by how the scattering mechanism within each TBG is, see Fig. 4(d). This signals that the usual compensation of the scattering time in the ratio $\sim \sigma_D/\sigma_1\sigma_2$ does not take place when the twist angles differ. To understand this behavior, in Fig. 5, we show the NLS in TBG and the product between them as it enters the drag conductivity kernel. The density plot in Fig. 5(a) shows the characteristic behavior of the NLS for $\tau \propto 1/k$ (see Fig. 2): it peaks around $v^\star q = \omega$, from which it decreases in magnitude as $|v^\star q - \omega| > 0$, until it becomes zero at certain lines along each side of $v^\star q = \omega$, from which the NLS then increases and decreases again with an opposite sign. This change of sign in the NLS arises due to an inverse energy dependence of the scattering time [29] (it does not occur for, e.g., a constant scattering time or $\tau \propto k$).

The consequences of such behavior in the drag effect can then be intuitively understood by analyzing Figs. 5(c) and 5(d), which show a momentum cut at $q/k_F = 1$ of the product of two NLSs, in the case of (c), equal twist angles and (d) different twist angles. In the first case, since the NLS product $\sim\Gamma^2$ is always positive, the change of sign as each NLS decreases away from $v^\star q = \omega$ is only seen as small peaks at each side of it. In contrast, the product of two NLSs with different twist angles yields regions at which the result is negative and, more importantly, where it changes sign between its peaks. This holds in general, with different weight, for any value of q. Since all other quantities that determine σ_D in Eq. (1) are positive, the net effect of a change of sign in the

product $\Gamma_1\Gamma_2$ is to lower or raise the drag resistivity, depending on the relation between θ_1 and θ_2. It is interesting to note that sign reversals in the drag resistivity, without a change of carrier type in each layer, have been measured in electron-hole double bilayer graphene systems [63,64] and attributed to a multiband mechanism that can change the sign of the product of two NLSs [65]. Here, we emphasize that such behavior is a direct consequence of the momentum-dependence of the scattering time in TBG.

IV. CONCLUSIONS

We have studied the Coulomb drag between two metallic TBGs separated so that they only couple through long-range Coulomb interactions. The drag resistivity is calculated considering the contributions of gauge phonons and charged impurities to the scattering in TBG. The proposed drag setup assumes that the twist angle in each TBG can be varied independently. In the case of equal twist angles, the drag resistivity follows the expected behavior of exhibiting a unique maximum as the system crosses over from a degenerate to a nondegenerate regime. This crossover can take place solely by varying the twist angle. When the twist angles in each TBG differ, we have found an anomalous drag effect, characterized by the appearance of multiple peaks that depend on the difference between the angles as well as other parameters of the system. This behavior arises from sign changes in the product of two nonlinear susceptibilities with different twist angles, where due to the momentum dependence of the scattering time in metallic TBG, the result can be negative or positive depending on the difference between the twist angles. Such a change of sign influences the magnitude of the drag conductivity and leads to a nonmonotonic drag effect.

ACKNOWLEDGMENTS

This paper was partially supported by grants of the Argentina National Research Council (CONICET) and Universidad Nacional del Sur and by ANPCyT through PICT 2019-03491 Res. No. 015/2021, and PIP-CONICET 2021-2023 Grant No. 11220200100941CO. J.S.A. acknowledges support as a member of CONICET, F.E. acknowledges support from a research fellowship from this institution.

APPENDIX A: NLS FOR ISOTROPIC SCATTERING TIME

In this Appendix, we give details of the calculation of the NLS given by Eq. (8), assuming an isotropic scattering time $\tau_{\ell,\mathbf{k}} = \tau_\ell(|\mathbf{k}|)$. Following Eq. (1), we only compute the NLS for $\omega > 0$. Within the two-band Dirac approximation of TBG (Sec. II B), we have

$$\epsilon_{\ell,\mathbf{k},s} = s\hbar v^\star_\ell |\mathbf{k}|, \quad \mathbf{v}_{\ell,\mathbf{k},s} = s v^\star_\ell \hat{\mathbf{k}}, \tag{A1}$$

$$F_{ss'}(\mathbf{k},\mathbf{q}) = \frac{1}{2}\left[1 + ss'\frac{k + q\cos\left(\varphi_{\mathbf{k}} - \varphi_{\mathbf{q}}\right)}{|\mathbf{k}+\mathbf{q}|}\right]. \tag{A2}$$

We separate $\mathbf{\Gamma}_\ell(\mathbf{q},\omega) = \sum_{s,s'} \mathbf{\Gamma}_{\ell,s,s'}(\mathbf{q},\omega)$. By introducing the change of angle $\varphi = \varphi_{\mathbf{k}} - \varphi_{\mathbf{q}}$, the Dirac delta in the NLS can be resolved as

$$\delta(\hbar\omega + \epsilon_{\ell,\mathbf{k},s} - \epsilon_{\ell,\mathbf{k}+\mathbf{q},s'}) = \frac{2}{\hbar v^\star_\ell}\frac{|\omega_\ell + sk|\sum_{i=0,1}\delta(\varphi-\varphi_i)}{\sqrt{\left(q^2-\omega_\ell^2\right)[(\omega_\ell+2sk)^2-q^2]}}, \tag{A3}$$

where $\varphi_1 = 2\pi - \varphi_0$ with $\cos\varphi_0 = (\omega_\ell^2 + 2sk\omega_\ell - q^2)/2kq$. Then in Eq. (8), we have

$$(\tau_{\ell,\mathbf{k}}\mathbf{v}_{\mathbf{k},s} - \tau_{\ell,\mathbf{k}+\mathbf{q}}\mathbf{v}_{\ell,\mathbf{k}+\mathbf{q},s'}) \to -sv^\star_\ell\frac{\mathbf{q}}{2q^2}\frac{1}{k+s\omega_\ell}\frac{1}{k}Y_{ss'}(q,\omega_\ell,k), \tag{A4}$$

where

$$Y_{ss'}(q,\omega,k) = \tau[s'(\omega+sk)]k(q^2+\omega^2+2sk\omega) + \tau(k)(k+s\omega)(q^2-\omega^2-2sk\omega). \tag{A5}$$

In the above, we have used that $\mathbf{k} = \mathbf{q}(k/q)\cos\varphi + (\mathbf{e}_z\times\mathbf{q})(k/q)\sin\varphi$, and we have dropped terms proportional to $\sin\varphi$ because they vanish after the integration over the angle [cf. Eq. (A3)]. Resolving the angle integration by imposing the restrictions $|\cos\varphi_0| < 1$ and $\omega > 0$, we find

$$\mathbf{\Gamma}_{\ell,-,-}(\mathbf{q},\omega{>}0) = -\frac{g}{4\pi\hbar}\Theta(q-\omega_\ell)\frac{\mathbf{q}}{\sqrt{|q^2-\omega_\ell^2|}}\frac{1}{q^2} \times\int_{(q+\omega_\ell)/2}^{\infty} dk I_-(q,\omega_\ell,k)Y_{--}(q,\omega_\ell,k), \tag{A6}$$

$$\mathbf{\Gamma}_{\ell,-,+}(\mathbf{q},\omega>0) = -\frac{g}{4\pi\hbar}\Theta(\omega_\ell-q)\frac{\mathbf{q}}{\sqrt{|q^2-\omega_\ell^2|}}\frac{1}{q^2} \times\int_{(\omega_\ell-q)/2}^{(\omega_\ell+q)/2} dk I_-(q,\omega_\ell,k)Y_{-+}(q,\omega_\ell,k), \tag{A7}$$

$$\mathbf{\Gamma}_{\ell,+,-}(\mathbf{q},\omega>0) = 0, \tag{A8}$$

$$\mathbf{\Gamma}_{\ell,+,+}(\mathbf{q},\omega>0) = \frac{g}{4\pi\hbar}\Theta(q-\omega_\ell)\frac{\mathbf{q}}{\sqrt{|q^2-\omega_\ell^2|}}\frac{1}{q^2} \times\int_{(q-\omega_\ell)/2}^{\infty} dk I_+(q,\omega_\ell,k)Y_{++}(q,\omega_\ell,k), \tag{A9}$$

where

$$I_\pm(q,\omega,k) = [f_\ell(\pm k) - f_\ell(\omega\pm k)] \times\sqrt{|(\omega\pm 2k)^2-q^2|}\frac{1}{k(k+\omega)}. \tag{A10}$$

From here, Eq. (9) follows after rewriting the k integrals by changing variables and regrouping terms.

APPENDIX B: DYNAMICAL SCREENING AND COLLINEAR SINGULARITY

The collinear singularity, within the Dirac approximation, gives rise to the divergences in the NLS when $v^\star_\ell q \to \omega$ [22]. Here, we show that these divergences are cured in the calculation of the drag conductivity when the dynamical screening

of the interlayer interaction is considered [52]. We start by writing the effective dielectric function in Eq. (14) as

$$\varepsilon_{12}(q,\omega)=\left(1+\frac{q_1}{q}\right)\left(1+\frac{q_2}{q}\right)-\frac{q_1q_2}{q^2}e^{-2qd}. \tag{B1}$$

Here, we defined an effective TF wave vector $q_\ell = q_{R,\ell} + iq_{I,\ell}$ in the TBG $\ell = 1, 2$, where $q_{R/I,\ell} = q_{0T,\ell}\tilde{\Pi}_{R/I,\ell}$, with $q_{0T,\ell} = g\alpha_\ell k_{F,\ell}$ being the zero temperature TF vector, and $\tilde{\Pi}_{R/I,\ell} = \Pi_{R/I,\ell}/D_0$ the real and imaginary parts of the polarization function in Eq. (15), scaled by the density of states $D_0 = gk_{F,\ell}/2\pi\hbar v^\star_\ell$. To compute $\tilde{\Pi}_R$ and $\tilde{\Pi}_I$, we use the semi-analytical expressions of Ref. [61], which for $\omega > 0$ can be written as

$$\tilde{\Pi}_{R,\ell}=\frac{k_BT}{E_{F,\ell}}\mathcal{F}_\ell-\frac{q}{4k_{F,\ell}}\frac{1}{\sqrt{|1-\omega_\ell^2/q^2|}}[\Theta(\omega_\ell-q)\mathcal{G}_\ell(q,\omega,T)+\Theta(q-\omega_\ell)\mathcal{H}_\ell(q,\omega,T)], \tag{B2}$$

$$\tilde{\Pi}_{I,\ell}=\frac{q}{4k_{F,\ell}}\frac{1}{\sqrt{|1-\omega_\ell^2/q^2|}}[\Theta(q-\omega_\ell)\mathcal{G}_\ell(q,\omega,T)-\Theta(\omega_\ell-q)\mathcal{H}_\ell(q,\omega,T)], \tag{B3}$$

where $\mathcal{F}_\ell = \ln[2(1+\cosh\beta\mu_\ell)]$, and

$$\mathcal{G}_\ell(q,\omega,T)=\sum_{a,b=\pm1}\int_1^\infty du\frac{a\sqrt{u^2-1}}{\exp[(\hbar|v^\star_\ell qu-a\omega|+2b\mu_\ell)/2k_BT]+1}, \tag{B4}$$

$$\mathcal{H}_\ell(q,\omega,T)=-\frac{\pi}{2}+\sum_{a,b=\pm1}\int_0^1\times du\frac{\sqrt{1-u^2}}{\exp[(\hbar|v^\star_\ell qu-a\omega|+2b\mu_\ell)/2k_BT]+1}. \tag{B5}$$

Now we redefine

$$\tilde{\Pi}_{R/I,\ell}\to\frac{1}{\sqrt{|1-\omega_\ell^2/q^2|}}\tilde{\Pi}_{R/I,\ell}, \tag{B6}$$

which in turn implies $q_{R/I,\ell}\to\tilde{q}_{R/I,\ell}[1-\omega_\ell^2/q^2]^{-1/2}$. The dielectric function can then be written as

$$\varepsilon_{12}(q,\omega)=\frac{\tilde{\varepsilon}_{12}(q,\omega)}{q^2\sqrt{|1-\omega_1^2/q^2||1-\omega_2^2/q^2|}}, \tag{B7}$$

where

$$\tilde{\varepsilon}_{12}(q,\omega)=\left(q\sqrt{|1-\omega_1^2/q^2|}+\tilde{q}_1\right)\left(q\sqrt{|1-\omega_2^2/q^2|}+\tilde{q}_2\right)-\tilde{q}_1\tilde{q}_2e^{-2qd}, \tag{B8}$$

with $\tilde{q}_\ell = \tilde{q}_{R,\ell} + i\tilde{q}_{I,\ell}$. The divergences now only appear in the denominator of Eq. (B7). By replacing $\varepsilon_{12}(q,\omega)$ above and the projected NLS given by Eq. (9) (choosing the current in the x axis), the drag conductivity in Eq. (1) becomes

$$\sigma_D=\frac{e^2}{h}\frac{g^2}{64\pi}\frac{\hbar}{k_BT}\alpha_1^\star\alpha_2^\star v_1^\star v_2^\star\int dq\frac{e^{-2qd}}{q}\times\int_0^\infty d\omega\frac{\sqrt{|1-\omega_1^2/q^2|}\sqrt{|1-\omega_2^2/q^2|}}{|\tilde{\varepsilon}_{12}(q,\omega)|^2}\times\frac{\Gamma_1(q,\omega)\Gamma_2(q,\omega)}{\sinh^2(\hbar\omega/2k_BT)}, \tag{B9}$$

where

$$\Gamma_\ell(q,\omega)=\Theta(q-\omega_\ell)\Gamma_{\ell,+}(q,\omega)+\Theta(\omega_\ell-q)\Gamma_{\ell,-}(q,\omega). \tag{B10}$$

The expression in Eq. (B9) explicitly shows that the divergences in both the dielectric function and the NLS, when $v^\star_\ell q\to\omega$, are effectively cured in the integral kernel.

[1] Y. Cao, V. Fatemi, S. Fang, K. Watanabe, T. Taniguchi, E. Kaxiras, and P. Jarillo-Herrero, Unconventional superconductivity in magic-angle graphene superlattices, Nature (London) **556**, 43 (2018).

[2] Y. Cao, V. Fatemi, A. Demir, S. Fang, S. L. Tomarken, J. Y. Luo, J. D. Sanchez-Yamagishi, K. Watanabe, T. Taniguchi, E. Kaxiras *et al.*, Correlated insulator behaviour at half-filling in magic-angle graphene superlattices, Nature (London) **556**, 80 (2018).

[3] M. Yankowitz, S. Chen, H. Polshyn, Y. Zhang, K. Watanabe, T. Taniguchi, D. Graf, A. F. Young, and C. R. Dean, Tuning superconductivity in twisted bilayer graphene, Science **363**, 1059 (2019).

[4] D. Wong, K. P. Nuckolls, M. Oh, B. Lian, Y. Xie, S. Jeon, K. Watanabe, T. Taniguchi, B. A. Bernevig, and A. Yazdani, Cascade of electronic transitions in magic-angle twisted bilayer graphene, Nature (London) **582**, 198 (2020).

[5] M. Oh, K. P. Nuckolls, D. Wong, R. L. Lee, X. Liu, K. Watanabe, T. Taniguchi, and A. Yazdani, Evidence for unconventional superconductivity in twisted bilayer graphene, Nature (London) **600**, 240 (2021).

[6] A. T. Pierce, Y. Xie, J. M. Park, E. Khalaf, S. H. Lee, Y. Cao, D. E. Parker, P. R. Forrester, S. Chen, K. Watanabe *et al.*, Unconventional sequence of correlated Chern insulators in magic-angle twisted bilayer graphene, Nat. Phys. **17**, 1210 (2021).

[7] J. M. B. Lopes dos Santos, N. M. R. Peres, and A. H. Castro Neto, Graphene bilayer with a twist: Electronic structure, Phys. Rev. Lett. **99**, 256802 (2007).

[8] S. Shallcross, S. Sharma, E. Kandelaki, and O. A. Pankratov, Electronic structure of turbostratic graphene, Phys. Rev. B **81**, 165105 (2010).

[9] A. Luican, G. Li, A. Reina, J. Kong, R. R. Nair, K. S. Novoselov, A. K. Geim, and E. Y. Andrei, Single-layer behavior and its breakdown in twisted graphene layers, Phys. Rev. Lett. **106**, 126802 (2011).

[10] R. Bistritzer and A. H. MacDonald, Moiré bands in twisted double-layer graphene, Proc. Natl. Acad. Sci. USA **108**, 12233 (2011).

[11] G. Tarnopolsky, A. J. Kruchkov, and A. Vishwanath, Origin of magic angles in twisted bilayer graphene, Phys. Rev. Lett. **122**, 106405 (2019).

[12] A. Nimbalkar and H. Kim, Opportunities and challenges in twisted bilayer graphene: A review, Nano-Micro Lett. **12**, 126 (2020).

[13] E. Y. Andrei and A. H. MacDonald, Graphene bilayers with a twist, Nat. Mater. **19**, 1265 (2020).

[14] X. Liu, Z. Wang, K. Watanabe, T. Taniguchi, O. Vafek, and J. I. A. Li, Tuning electron correlation in magic-angle twisted bilayer graphene using coulomb screening, Science **371**, 1261 (2021).

[15] G. Wagner, Y. H. Kwan, N. Bultinck, S. H. Simon, and S. A. Parameswaran, Global phase diagram of the normal state of twisted bilayer graphene, Phys. Rev. Lett. **128**, 156401 (2022).

[16] W. Chen, Y. Chu, T. Huang, and T. Ma, Metal-insulator transition and dominant $d + id$ pairing symmetry in twisted bilayer graphene, Phys. Rev. B **101**, 155413 (2020).

[17] T.-F. Chung, Y. Xu, and Y. P. Chen, Transport measurements in twisted bilayer graphene: Electron-phonon coupling and Landau level crossing, Phys. Rev. B **98**, 035425 (2018).

[18] M. Anđelković, L. Covaci, and F. M. Peeters, DC conductivity of twisted bilayer graphene: Angle-dependent transport properties and effects of disorder, Phys. Rev. Mater. **2**, 034004 (2018).

[19] H. Polshyn, M. Yankowitz, S. Chen, Y. Zhang, K. Watanabe, T. Taniguchi, C. R. Dean, and A. F. Young, Large linear-in-temperature resistivity in twisted bilayer graphene, Nat. Phys. **15**, 1011 (2019).

[20] F. Wu, E. Hwang, and S. Das Sarma, Phonon-induced giant linear-in-T resistivity in magic angle twisted bilayer graphene: Ordinary strangeness and exotic superconductivity, Phys. Rev. B **99**, 165112 (2019).

[21] A. G. Rojo, Electron-drag effects in coupled electron systems, J. Phys.: Condens. Matter **11**, R31 (1999).

[22] B. N. Narozhny and A. Levchenko, Coulomb drag, Rev. Mod. Phys. **88**, 025003 (2016).

[23] T. J. Gramila, J. P. Eisenstein, A. H. MacDonald, L. N. Pfeiffer, and K. W. West, Evidence for virtual-phonon exchange in semiconductor heterostructures, Phys. Rev. B **47**, 12957 (1993).

[24] M. C. Bønsager, K. Flensberg, B. Y.-K. Hu, and A. H. MacDonald, Frictional drag between quantum wells mediated by phonon exchange, Phys. Rev. B **57**, 7085 (1998).

[25] O. L. Berman, R. Y. Kezerashvili, and Y. E. Lozovik, Drag effects in a system of electrons and microcavity polaritons, Phys. Rev. B **82**, 125307 (2010).

[26] F. Escudero and J. S. Ardenghi, Cavity-mediated drag in double-layer graphene, J. Phys.: Condens. Matter **34**, 395602 (2022).

[27] B. N. Narozhny, M. Titov, I. V. Gornyi, and P. M. Ostrovsky, Coulomb drag in graphene: Perturbation theory, Phys. Rev. B **85**, 195421 (2012).

[28] I. Yudhistira, N. Chakraborty, G. Sharma, D. Y. H. Ho, E. Laksono, O. P. Sushkov, G. Vignale, and S. Adam, Gauge-phonon dominated resistivity in twisted bilayer graphene near magic angle, Phys. Rev. B **99**, 140302(R) (2019).

[29] G. Sharma, I. Yudhistira, N. Chakraborty, D. Y. H. Ho, M. M. A. Ezzi, M. S. Fuhrer, G. Vignale, and S. Adam, Carrier transport theory for twisted bilayer graphene in the metallic regime, Nat. Commun. **12**, 5737 (2021).

[30] L. Cai and G. Yu, Fabrication strategies of twisted bilayer graphenes and their unique properties, Adv. Mater. **33**, 2004974 (2021).

[31] H. Yang, L. Liu, H. Yang, Y. Zhang, X. Wu, Y. Huang, H.-J. Gao, and Y. Wang, Advance in two-dimensional twisted moiré materials: Fabrication, properties, and applications, Nano Res. **16**, 2579 (2023).

[32] H.-Z. Zhang, W.-J. Wu, L. Zhou, Z. Wu, and J. Zhu, Steering on degrees of freedom of 2D van der Waals heterostructures, Small Sci. **2**, 2100033 (2022).

[33] M. Liu, L. Wang, and G. Yu, Developing graphene-based moiré heterostructures for twistronics, Adv. Sci. **9**, 2103170 (2022).

[34] C. Cao, T. Wu, and Y. Sun, A review of assembly techniques for fabricating twisted bilayer graphene, J. Micromech. Microeng. **31**, 114004 (2021).

[35] D. M. Kennes, M. Claassen, L. Xian, A. Georges, A. J. Millis, J. Hone, C. R. Dean, D. N. Basov, A. N. Pasupathy, and A. Rubio, Moiré heterostructures as a condensed-matter quantum simulator, Nat. Phys. **17**, 155 (2021).

[36] A. Kamenev and Y. Oreg, Coulomb drag in normal metals and superconductors: Diagrammatic approach, Phys. Rev. B **52**, 7516 (1995).

[37] K. Flensberg, B. Y.-K. Hu, A.-P. Jauho, and J. M. Kinaret, Linear-response theory of Coulomb drag in coupled electron systems, Phys. Rev. B **52**, 14761 (1995).

[38] A.-P. Jauho and H. Smith, Coulomb drag between parallel two-dimensional electron systems, Phys. Rev. B **47**, 4420 (1993).

[39] E. H. Hwang, R. Sensarma, and S. Das Sarma, Coulomb drag in monolayer and bilayer graphene, Phys. Rev. B **84**, 245441 (2011).

[40] J. Lux and L. Fritz, Kinetic theory of Coulomb drag in two monolayers of graphene: From the Dirac point to the Fermi liquid regime, Phys. Rev. B **86**, 165446 (2012).

[41] F. Escudero, F. Arreyes, and J. S. Ardenghi, Coulomb drag between two graphene layers at different temperatures, Phys. Rev. B **106**, 245414 (2022).

[42] B. A. Bernevig, Z.-D. Song, N. Regnault, and B. Lian, Twisted bilayer graphene. I. Matrix elements, approximations, perturbation theory, and a $k \cdot p$ two-band model, Phys. Rev. B **103**, 205411 (2021).

[43] A. H. Castro Neto, F. Guinea, N. M. R. Peres, K. S. Novoselov, and A. K. Geim, The electronic properties of graphene, Rev. Mod. Phys. **81**, 109 (2009).

[44] S. K. Jain, V. Juričić, and G. T. Barkema, Structure of twisted and buckled bilayer graphene, 2D Mater. **4**, 015018 (2016).

[45] M. Koshino and N. N. T. Nam, Effective continuum model for relaxed twisted bilayer graphene and moiré electron-phonon interaction, Phys. Rev. B **101**, 195425 (2020).

[46] S. Das Sarma, S. Adam, E. H. Hwang, and E. Rossi, Electronic transport in two-dimensional graphene, Rev. Mod. Phys. **83**, 407 (2011).

[47] M. Zarenia, I. Yudhistira, S. Adam, and G. Vignale, Enhanced hydrodynamic transport in near magic angle twisted bilayer graphene, Phys. Rev. B **101**, 045421 (2020).

[48] E. H. Hwang and S. Das Sarma, Screening-induced temperature-dependent transport in two-dimensional graphene, Phys. Rev. B **79**, 165404 (2009).

[49] B. Lian, Z. Wang, and B. A. Bernevig, Twisted bilayer graphene: A phonon-driven superconductor, Phys. Rev. Lett. **122**, 257002 (2019).

[50] E. H. Hwang and S. Das Sarma, Impurity-scattering-induced carrier transport in twisted bilayer graphene, Phys. Rev. Res. **2**, 013342 (2020).

[51] B. Amorim and N. M. R. Peres, On Coulomb drag in double layer systems, J. Phys.: Condens. Matter **24**, 335602 (2012).

[52] M. Carrega, T. Tudorovskiy, A. Principi, M. I. Katsnelson, and M. Polini, Theory of Coulomb drag for massless Dirac fermions, New J. Phys. **14**, 063033 (2012).

[53] S. M. Badalyan and F. M. Peeters, Enhancement of Coulomb drag in double-layer graphene structures by plasmons and dielectric background inhomogeneity, Phys. Rev. B **86**, 121405(R) (2012).

[54] R. Fandan, J. Pedrós, F. Guinea, A. Boscá, and F. Calle, Effect of quasiparticle excitations and exchange-correlation in Coulomb drag in graphene, Commun. Phys. **2**, 158 (2019).

[55] S. Gangadharaiah, A. M. Farid, and E. G. Mishchenko, Charge response function and a novel plasmon mode in graphene, Phys. Rev. Lett. **100**, 166802 (2008).

[56] V. N. Kotov, B. Uchoa, V. M. Pereira, F. Guinea, and A. H. Castro Neto, Electron-electron interactions in graphene: Current status and perspectives, Rev. Mod. Phys. **84**, 1067 (2012).

[57] N. M. R. Peres, J. M. B. Lopes dos Santos, and A. H. Castro Neto, Coulomb drag and high-resistivity behavior in double-layer graphene, EPL **95**, 18001 (2011).

[58] G. D. Mahan, *Many-Particle Physics*, 3rd ed. (Springer, New York, 2000).

[59] M. I. Katsnelson, Coulomb drag in graphene single layers separated by a thin spacer, Phys. Rev. B **84**, 041407(R) (2011).

[60] K. Flensberg and B. Y.-K. Hu, Plasmon enhancement of Coulomb drag in double-quantum-well systems, Phys. Rev. B **52**, 14796 (1995).

[61] M. R. Ramezanali, M. M. Vazifeh, R. Asgari, M. Polini, and A. H. MacDonald, Finite-temperature screening and the specific heat of doped graphene sheets, J. Phys. A: Math. Theor. **42**, 214015 (2009).

[62] W. Chen, A. V. Andreev, and A. Levchenko, Boltzmann-Langevin theory of Coulomb drag, Phys. Rev. B **91**, 245405 (2015).

[63] K. Lee, J. Xue, D. C. Dillen, K. Watanabe, T. Taniguchi, and E. Tutuc, Giant frictional drag in double bilayer graphene heterostructures, Phys. Rev. Lett. **117**, 046803 (2016).

[64] J. I. A. Li, T. Taniguchi, K. Watanabe, J. Hone, A. Levchenko, and C. R. Dean, Negative Coulomb drag in double bilayer graphene, Phys. Rev. Lett. **117**, 046802 (2016).

[65] M. Zarenia, A. R. Hamilton, F. M. Peeters, and D. Neilson, Multiband mechanism for the sign reversal of coulomb drag observed in double bilayer graphene heterostructures, Phys. Rev. Lett. **121**, 036601 (2018).